Article

Experimental Investigation of Failure Mechanisms of Granites with Prefabricated Cracks Induced by Cyclic-Impact Disturbances

Jie Zhang [1], Xun Xi [1,2], Wenhui Tan [1,*], Xu Wu [3], Xinghui Wu [1], Qifeng Guo [1] and Meifeng Cai [1]

1 School of Civil and Resource Engineering, University of Science and Technology Beijing, Beijing 100083, China; zhangjie@xs.ustb.edu.cn (J.Z.); xun.xi@strath.ac.uk (X.X.); wuxinghui@xs.ustb.edu.cn (X.W.); guoqifeng@ustb.edu.cn (Q.G.); caimeifeng@ustb.edu.cn (M.C.)
2 Civil and Environmental Engineering, University of Strathclyde, Glasgow G1 1XJ, UK
3 Beijing Municipal Engineering Research Institute, Beijing 100037, China; bjshizhengwuxu@hotmail.com
* Correspondence: wenhui.t@163.com

Abstract: Engineering rock mass is normally subject to cyclic–dynamic disturbances from excavation, blasting, drilling, and earthquakes. Natural fractures in rock masses can be reactivated and propagated under dynamic and static loadings, which affects the stability of rock mass engineering. However, fractured rock mass failure induced by cyclic-impact disturbances is far from clear, especially considering varying angles between the rock mass and the direction of impact loadings. This work investigated rock deformation and failure characteristics through cyclic impact tests on granite samples with cracks of different angles. A Hopkinson bar was employed for uniaxial cyclic impact tests on granite samples with the crack inclination angles of 0–90°. The magnetic resonance imaging technique was used to determine rocks' porosity after cyclic impacts. The stress–strain curves, porosity, strength, deformation modulus, failure modes, and energy density of samples were obtained and discussed. Results showed that the crack inclination angles significantly affected the damage evolution and crack morphology of rocks. Under the constant cyclic impact, the dynamic deformation modulus and dynamic strength of rock samples first increased and then decreased with the increase in crack inclination angle. The failures of granite samples for inclination angles of 0 and 90° were dominated by tensile cracking, while those for the inclination angles of 30–60° were dominated by shear cracking. The energy density per unit time gradually decreased with the increase in impact cycles. The results can provide references for the stability analysis and cyclic-impact-induced failure prediction of fractured rock masses.

Keywords: cyclic impacts; fractured rock mass; failure characteristics; crack propagation; dynamic deformation

1. Introduction

Large-scale rock mass projects with complex geological conditions continue to emerge with the rapid development of infrastructure construction in hydropower, transportation, railways, energy, and mining industries. Engineering rock masses are subject to dynamic disturbances such as blasting excavation, mechanical rock drilling, and earthquakes besides certain static loading [1–3]. The stability problem of surrounding rocks caused by cyclic-impact loading has always been an important research topic in rock mechanics and engineering circles at home and abroad. As a heterogeneous anisotropic medium, fractured rock masses have complex mechanical behaviors due to the random distribution of joint cracks [4]. Compared with intact rock masses, fractured ones are more sensitive to dynamic disturbance loads. The failure and instability of non-penetrating fractured rock masses is the process of internal weak-plane expansion and cracks' penetration. Therefore, it is of great importance to explore the damage characteristics and mechanism of fractured rock masses under dynamic disturbances for the stability of rock mass engineering structures.

The mechanics and failure characteristics of rocks under dynamic loadings are different from those under static loadings. Experts have achieved beneficial results after massive work. Li and Gong et al. [5–7] analyzed the dynamic mechanical properties of rocks under different static loadings by a dynamic–static loading test. Jin et al. [8] explored the fatigue mechanical properties of rocks under coupled static loadings and cyclic impacts to derive the effect of static loadings on the cumulative damage of rocks. Tian and Wang et al. [9,10] revealed the damage evolution mechanism of rocks by analyzing the effect of static axial compressions on the dynamic mechanical properties of granite samples under cyclic-impact loadings. For non-penetrating fractured rocks or rock-like materials, Liu et al. [11] discussed the peak intensity and failure mode of prefabricated jointed rock masses under the static uniaxial compression based on different inclination angles, penetration degrees, groups, and loading strain rates. Zhou et al. [12] quantitatively studied the effect of joint penetration on the mechanical properties of rock masses using the equivalent rock mass (ERM) technology based on micromechanics, thus revealing the penetrating mode of fractured rocks. Guo et al. [13] explored the relationship between the crack-initiation angle of composite fractures and the inclination angles of cracks in uniaxial compression tests on single-fractured rocks, examining natural granites. The maximum distortion energy theory was used to determine the initiation characteristic of single-fractured rocks under uniaxial loads. Zhou et al. [14] analyzed the crack initiation, propagation, and penetration mechanism and the brittle failure characteristics of open rock bridges. Sun et al. [15] studied the failure modes of joint-like rock masses under dynamic and static loadings using the indoor test and particle discrete element method, deriving the effect of joint inclination angles on failure modes under different loads. Wang et al. [16] used a dynamic loading system to analyze the instability and failure characteristics of rock samples at loading rates and the multiple angles of single and double cracks. Li et al. [17,18] explored the crack initiation law and failure mechanism of fractured rock masses based on the mechanical properties and deformation failure characteristics of deeply fractured granites under coupled static–dynamic loadings. The above studies focus on the mechanical properties and fracture characteristics under different loads rather than the progressive damage characteristics of fractured rock masses under cyclic-disturbance loads.

In deep rock mass engineering, rock masses are simultaneously subjected to static preloads (e.g., tectonic stress and self-weight stress) and dynamic disturbances caused by blasting loads, earthquakes, and excavation [19,20] (e.g., the interval pillars of mine stopes) (see Figure 1). In these projects, most cyclic disturbance loadings activate microcracks in rock masses for further extension, rather than directly promoting the destruction of surrounding rocks [16]. This work took five kinds of sample rocks with different inclination angles of prefabricated cracks in rock masses as the research objects. A cyclic impact test was conducted using the improved SHPB as a loading system to explore the progressive-failure characteristics and mechanism of fractured rocks under cyclic-disturbance loadings, providing a certain basis for the practice and stability evaluation of rock mass engineering.
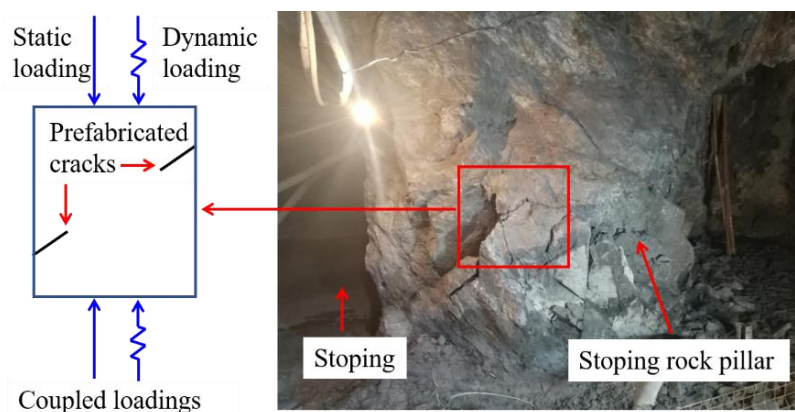
**Figure 1.** Fractured rock masses under coupled loadings.

2. Materials and Methods

2.1. Preparation of Specimens with Prefabricated Cracks

Based on the quasi-static compression test, the aspect ratio of rock samples was set to 2.0. In other words, rock samples were processed into a cylinder with a diameter of 50 mm and a height of 100 mm to explore the accumulative effects of impact disturbance failure and damage to rocks, thus presenting the pore changes of rock samples before and after impacts. Meanwhile, the aspect ratio did not affect the qualitative analysis of the impacts of crack inclination angles on dynamic strength under the same loading. The same batch of rocks was processed into standard cylindrical parts and cut with a water jet to prepare prefabricated cracks with a width of 0.3 mm. Both ends of sample rocks were polished to ensure that non-parallelism and non-perpendicularity were less than 0.02 mm.

The prefabricated cracks were located on both sides of rock samples, presenting symmetrical distribution. Crack inclination angle β refers to the angle between the connecting line of the crack tips on both sides and the horizontal direction ($\beta = 0°$, $30°$, $45°$, $60°$, and $90°$). Figure 2 shows a sample with prefabricated cracks. The connectivity rate is used to characterize the discontinuity of rock masses. Connectivity rate k of a crack surface refers to the ratio of the total area of the crack surface in the cross-section at a certain direction to the area of the entire cross-section. In the test, k is denoted as 0.35; for the area of prefabricated cracks on both sides, $S_1 = S_2$. After calculation of Equation (1), prefabricated crack length c of rock samples with different inclination angles is 11.5, 13.4, 16.3, 23.0, and 17.5 mm, respectively. Internal longitudinal-wave velocities of rock samples were measured to be 3430–3580 m/s by the ZBL-U5200 non-metallic ultrasonic detector. Sample rocks with different inclination angles have small dispersion of longitudinal-wave velocities. Intact rock samples without prefabricated cracks have an average longitudinal-wave velocity of 3590 m/s. This verifies that the internal structural defects of sample rocks with prefabricated cracks decrease the average longitudinal-wave velocity.

$$\text{Connectivity rate } (k) = \frac{\text{Crack area } (S_1 + S_2)}{\text{Cross-sectional area } (S_1 + S_2 + S_3)} \tag{1}$$


(a) (b)
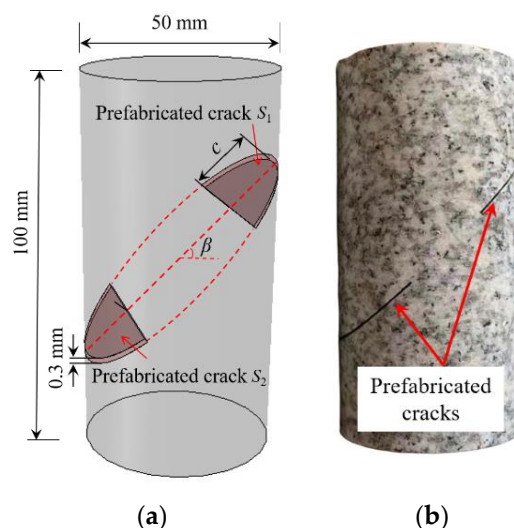
Figure 2. Granite sample with prefabricated cracks: (**a**) crack structure; (**b**) sample rock.

2.2. Experimental Equipment

2.2.1. Split Hopkinson Pressure Bar (SHPB)

The SHPB test can explore the dynamic properties of rocks. In the test, we used an SHPB device with a diameter of 50 mm in the impact laboratory of the University of Science and Technology Liaoning. Figure 3 shows the SHPB device. In the test system, a compressed nitrogen ejection device is applied to drive the warhead. The warhead and

the incident, transmission, and buffer bars are all made of high-strength 40Cr alloy steels. The longitudinal-wave velocity, elastic modulus, and uniaxial compressive strength are 5447 m/s, 240 GPa, and 800 MPa, respectively. All bars have diameters of 50 mm, and the warhead is the spindle pole body with a length of 360.1 mm; the incident, transmission, and buffer bars have lengths of 1800, 1800, and 1000 mm, respectively. BE120-SAA strain gauges are attached to the incident and transmission bars to collect the incident, reflected, and transmitted wave signals.
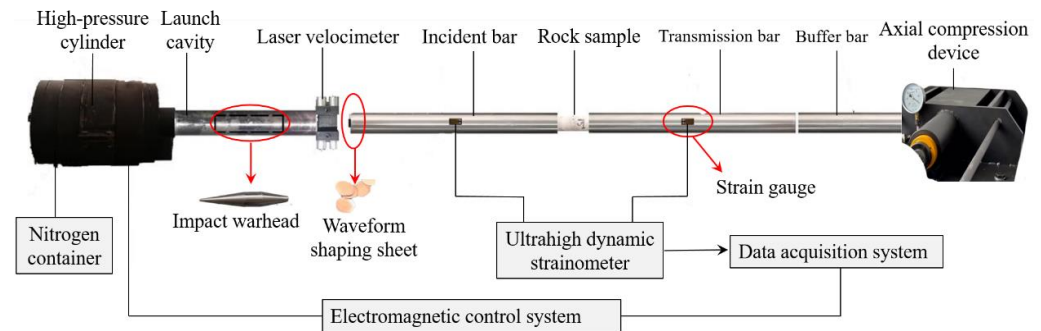
Figure 3. SHPB device.

The rock samples and the bar were impacted by loading the same cross-sectional area, and the loading wave was a half-sine pulse loaded with a constant strain rate. Before the test, the test system was calibrated with the empty bar impact test. The waveform diagram showed that the peak of the incident wave was the same as that of the transmitted wave; the reflected wave was 0, which met the basic requirements of the SHPB impact test. According to the one-dimensional stress wave theory, the collected strain-gauge voltage signals were conducted with data processing by the three-wave method to calculate the dynamic mechanical parameters such as stress, strain rate, and strain of rock samples [21].

$$\left.\begin{array}{l} \sigma(t) = \frac{A_0}{2A_s} E_0(\varepsilon_I + \varepsilon_R + \varepsilon_T) \\ \dot{\varepsilon}(t) = \frac{C_0}{L_s} E_0(\varepsilon_I - \varepsilon_R - \varepsilon_T) \\ \varepsilon(t) = \frac{C_0}{L_s} \int_0^t E_0(\varepsilon_I - \varepsilon_R - \varepsilon_T)\mathrm{d}t \end{array}\right\} \tag{2}$$

where A_0, E_0, and C_0 are the cross-sectional area, elastic modulus, and wave velocity of the pressure bar, respectively; ε_I, ε_R, and ε_T are the incident, reflection, and transmission strains measured on the incident and transmission bars, respectively; and L_s and A_s are the length and cross-sectional area of rock samples, respectively.

2.2.2. Nuclear Magnetic Resonance (NMR)

The NMR instrument used was the MacroMR12-150H-I large-aperture, nuclear-magnetic-resonance imaging analyzer from Shanghai Electronic Technology Co., Ltd. (Shanghai, China). It consists of a constant temperature system, industrial computer, supporting software, radio frequency unit, and gradient unit. The permanent magnet was made of Nd-Fe-B materials, where the magnetic field strength ranges from 0.25 to 0.35 T, the radio frequency transmission power > 300 W, the linear distortion degree < 0.005, and the resonance frequency = 12.63 MHz. The peripheral supporting equipment includes a ZYB-II vacuum pressure saturation device with a maximum pressure of 60 MPa.

The principle of NMR imaging is described as follows: First, the external-gradient magnetic field emitted multi-frequency electromagnetic waves to differentiate the attenuation of NMR signals of different structures in the substance. Then, the signal attenuation law was analyzed to understand the positions and types of internal structures, thus deriving the imaging of different internal structures. Before NMR imaging, rock specimens were saturated with water. The hydrogen nuclei concentrated on the internal defects, reflecting the joints and fissures with the distribution of pore water. More hydrogen nuclei in rocks lead to greater porosity. Rock damages caused by changes in pore structures are

quantitatively characterized by rocks' porosity, which can be expressed as the volume ratio of internal pores to rocks.

$$n = (V_k / V_Y) \cdot 100\%$$ (3)

where V_k is the total volume of pores and fissures in rock samples and V_Y is the volume of rock samples.

2.3. Experimental Protocol

2.3.1. Stress Loading Mode

In the test of cyclic-impact disturbances, rock samples were simultaneously subjected to axial static stress P_0 and dynamic impact loading P_d with a certain strength. After being subjected to multiple-impact disturbances, rock samples were destroyed. Figure 4 shows the stress-wave loading. During the test, axial static force P_0 = 8 MPa. The impact loading was adjusted repeatedly to ensure that rock samples were not heavily broken after several impacts, thus facilitating the NMR porosity test and imaging. Redundant fragments increased the errors of porosity measurement and the difficulty of the test.
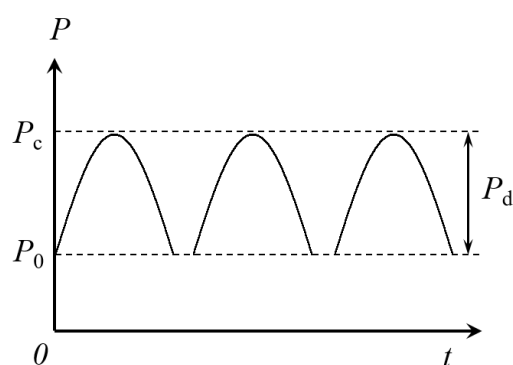

Figure 4. Stress-wave loading.

2.3.2. Impacting-Disturbance Strength

An appropriate impact intensity is key to the success of the test. The single impact loading should be within the dynamic damage threshold to realize the cyclic impact of rock samples. Rock samples have obvious damage accumulation, which is convenient for analyzing the progressive damage law. Scholars believed that the ratio of static initiation stress and peak strength of granites at low and medium strain rates has no obvious relationship with the strain rate. Crack volume–strain inflection points are used to determine initiation stress [22]. Wang et al. [10] proposed that dynamic initiation stress, as the damage threshold of cyclic impacts, is approximately equal to the product of the static initiation stress and the dynamic growth factor. It has not been verified that the ratio of dynamic initiation stress and compressive strength is rate-independent. In addition, the quasi-static damage strength excludes the rate effect of dynamic peak stress and strain. After taking energy per unit volume absorbed by rock samples to reach the static damage strength as the reference index for dynamic-impact damages, the appropriate impact strength is determined by the trial-and-error method. Under uniaxial compression, the rock sample with a crack inclination angle of 45° reaches static damage strength σ_{cd}. Absorbed energy per unit volume W_{cd} is the area below the static stress–strain curve (see Figure 5a). The amplitude of the dynamic-loading incident wave is controlled by adjusting the impact pressure. Rock samples with an inclination angle of 45° were tested with an impact test by adjusting pressures to 0.28, 0.23, and 0.20 MPa. Dynamic energy per unit volume W_{dc} is the area of the loading section of the dynamic stress–strain curve (see Figure 5b). Figure 6 shows the single-impact damage of rock samples.
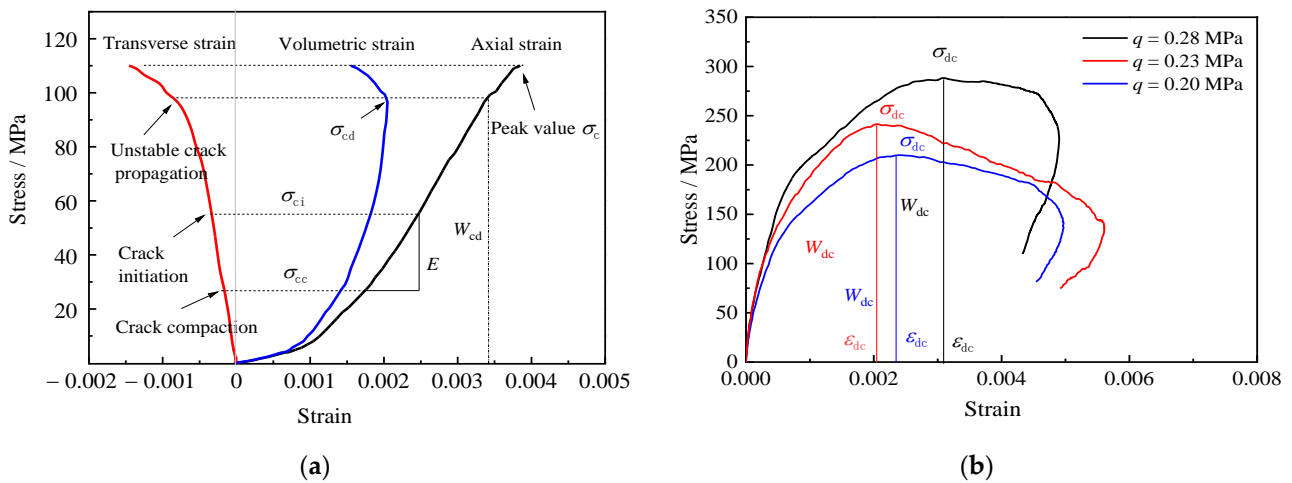
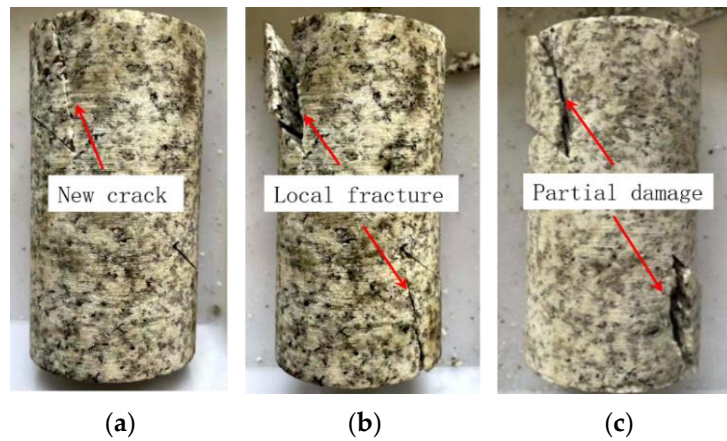**Figure 5.** Rocks' stress–strain curves: (**a**) static loading; (**b**) dynamic loading.

Figure 6. Degrees of fragmentation under different impact pressures: (**a**) q = 0.20 MPa; (**b**) q = 0.23 MPa; (**c**) q = 0.28 MPa.

The energy per unit volume at any point on the stress–strain curve is calculated by the definite integration method.

$$W_i = \int_0^{\varepsilon_i} \sigma_1 d\varepsilon_1 = \sum_{i=1}^n \frac{1}{2}(\sigma_{i+1} + \sigma_i)(\varepsilon_{i+1} - \varepsilon_i) \tag{4}$$

where σ_i and ε_i are stress and corresponding axial strain at any point of the stress–strain curve, respectively.

The calculation results showed that the energy per unit volume was absorbed by static damage W_{cd} = 0.1804 J/cm^3. If impacted air pressure $q \geq 0.23$ MPa, $W_{dc} > W_{cd}$; if q = 0.2 MPa, $W_{dc} < W_{cd}$. The impact pressure was not larger than 0.2 MPa to ensure that rock samples remained intact (without cracks) after the first impact. When the impacted air pressure was 0.20–0.23 MPa, prefabricated cracks of rock samples did not expand. When it was 0.28 MPa, the prefabricated cracks developed to the periphery, causing large damage (see Figure 6). Therefore, the cyclic impact air pressure was set to 0.18 MPa (the impact velocity = 10.07 m/s). There was no new crack in rock samples after the first impact. Samples were subjected to crack penetration failure after several cyclic impacts, which met the requirements of the cyclic-impact test.

2.3.3. Stress-Wave Propagation Characteristics

In the experiment, the incident wave loading lasted approximately 200 µs. The incident, reflected, and transmitted waves were half-sine waveforms. Figure 7 shows the waveforms

of granites at the same impact velocity in the SHPB test. The incident waves of multiple impacts have good coincidence, indicating the accurate control of the impact velocity.
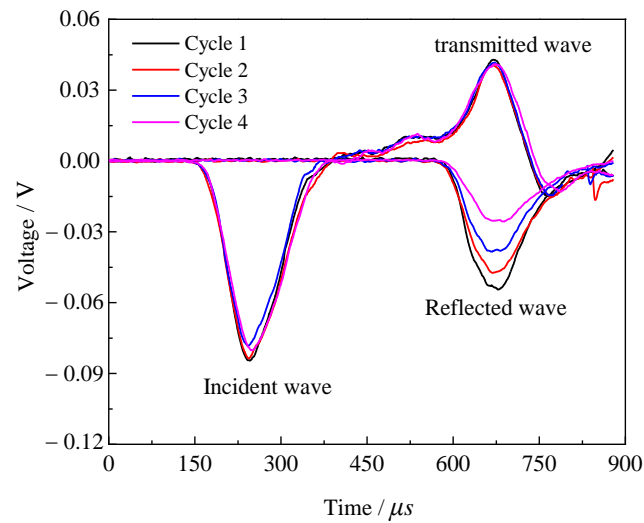
Figure 7. Waveforms of the cyclic-impact SHPB test of granite samples.

If the incident wave amplitude was constant, the reflected wave amplitude depended on the wave impedance of samples (ρ_c); the porosity was negatively correlated with density ρ and elastic-wave velocity c. The reflected and transmitted waves had coincident waveforms in the first two impacts, indicating that impacts caused weak damage to the rock at the previous stage where micropores and cracks were gestated. After that, the waveform significantly changed, indicating that the accumulated damages change the wave impedance of rocks. The transmitted wave amplitude reached the maximum in the first impact and decreased in subsequent impacts (see Figure 7). The damage degrees of rocks were different at the same impact velocity. The energy consumption of the rock's impact damage gradually increased. At the early stage, the rock had a small transmission wave amplitude and little energy consumption. After several impacts, damages accumulated, leading to the development of microcracks, which increased the energy consumption of damage to rocks.
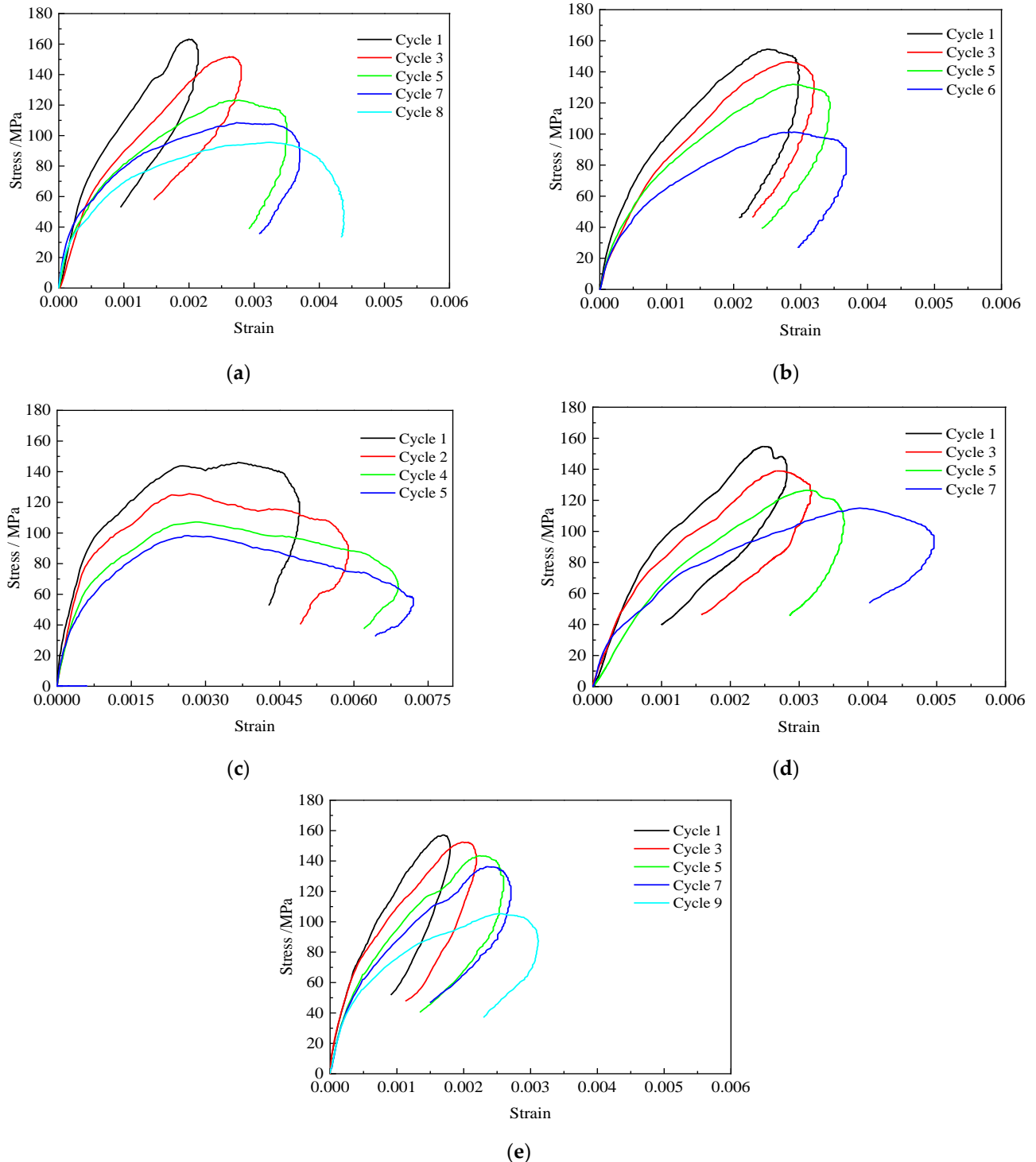
3. Results

3.1. Stress–Strain Curves

Figure 8 shows the stress–strain curves of rock samples with different crack inclination angles. The typical dynamic stress–strain curve obtained from the axial load–dynamic disturbance test has no compaction stage. The curves rise non-linearly before the dynamic stress peak and then rebound after the peak. Internal elastic energy of rocks releases at the peak when internal elastic force is greater than unloaded disturbance stress.

As shown in Figure 8, internal damages accumulate, which degrades the mechanical properties of rock samples with increased impacts. There are differences among the curves of rock samples with different crack inclination angles, indicating that the crack structure partly affects the impact resistance of rocks.

3.2. Dynamic Deformation Modulus

Under dynamic impact loads, rocks deform or even break instantaneously. Therefore, it is more accurate to characterize the dynamic deformation of rocks by dynamic deformation modulus. There is no explicit specification on determining deformation moduli of dynamic stress–strain curves at home and abroad. The secant modulus, second-type secant modulus, and loading deformation modulus are averaged to derive the dynamic deformation modulus, thus reflecting the compression deformation of rocks at the dynamic loading stage [23]. Figure 9 shows the relationship between the dynamic deformation
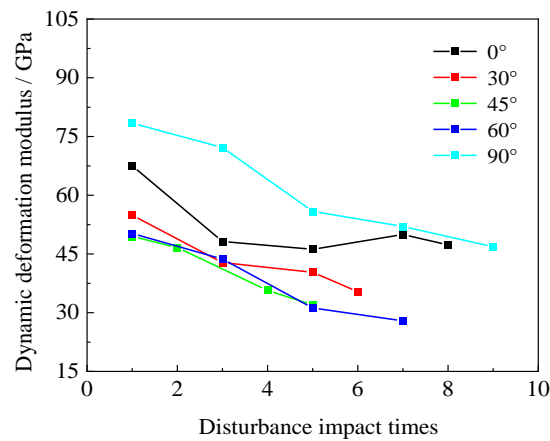
modulus and disturbance impact times at the loading stage based on different crack inclination angles. Generally, the dynamic deformation modulus decreases with the increase in impacts because of the cumulative evolution of internal damage during the disturbance impact. As impacts increase, the deformability to resist external loads decreases.

Figure 8. Stress–strain curves of rock samples with different crack inclination angles: (**a**) $\beta = 0°$; (**b**) $\beta = 30°$; (**c**) $\beta = 45°$; (**d**) $\beta = 60°$; (**e**) $\beta = 90°$.
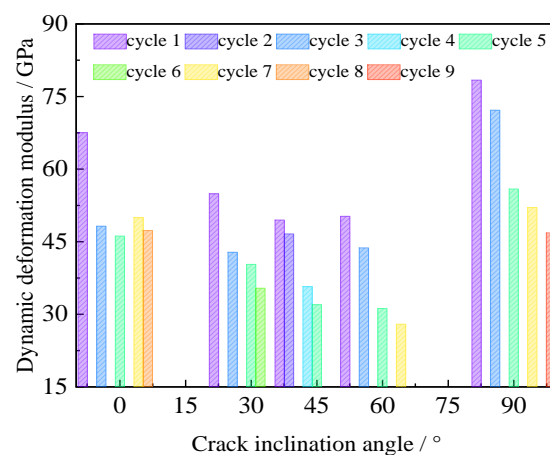
The dynamic deformation modulus of granites increases after decreasing with the increase in crack inclination angle (see Figure 9). The decreased rate of the dynamic deformation modulus also changes under cyclic impacts because of different internal

structures of rock samples with prefabricated cracks. A smaller dynamic deformation modulus of rocks leads to a weaker resistance to impact deformation to a certain extent. For rock samples with crack inclination angles of 0–30°, the deformation modulus has a larger reduction amplitude than the previous impacts. The reason may be that rock samples with small inclination angles have small crack lengths. Therefore, prefabricated cracks first close under cyclic-impact loads. When prefabricated cracks with an inclination angle of 0° are completely closed, the stress wave can be transmitted without reflection, which inhibits the deterioration of material [24] and increases deformation moduli in the next impact.

Figure 9. Relationship between the dynamic deformation modulus and disturbance impact times.

Figure 10 shows the relationship between the dynamic deformation modulus and the inclination angles of rock samples with prefabricated cracks. Rock samples with a crack inclination angle of 45° are firstly damaged after five impacts. The inclination angle and axial loading are more conducive to the development of cracks. Rock samples with an inclination angle of 30° have a slightly greater reduction in deformation moduli than those with an inclination angle of 60°. Rock samples with inclination angles of 0° and 90° have strong impact resistance. With the strongest impact resistance, rock samples with an inclination angle of 90° are least affected by prefabricated cracks. Therefore, their strength is close to the strength of intact rocks.
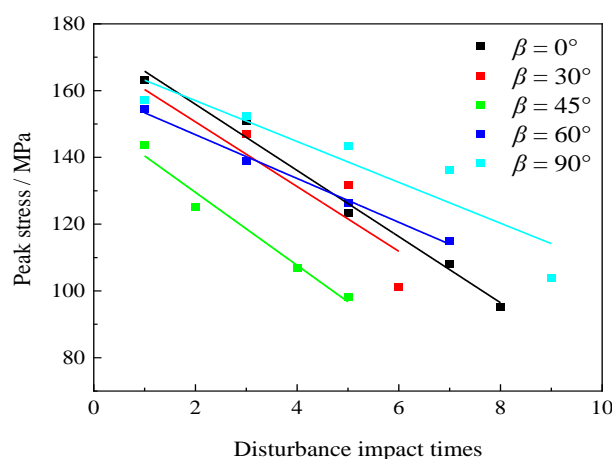

Figure 10. Relationship between dynamic deformation moduli and crack inclination angles.

3.3. Dynamic Peak Stress

The average peak stress in the impact of disturbance is defined as the average strength of rocks against impact disturbances. Results show that the average strength of rocks increases after decreasing with the increase in crack inclination angle. According to the relationship between the average strength and crack inclination angle, we can determine

the safety strength to withstand multiple disturbance impacts under a certain axial pressure. When the impact strength of disturbances exceeds the average strength, rocks are subjected to fewer impacts and are prone to damage. When the impact strength of disturbances is lower than the average strength, rocks not prone to damage are subjected to more impacts of disturbances.

Figure 11 shows the relationship between dynamic peak stress under frequent disturbances and the impact times of disturbance based on the same axial and impact pressures. The dynamic peak stress decreases linearly with the increase in disturbance impacts. The dynamic peak stress of rock samples with different crack inclination angles increases after decreasing with the increase in inclination angle. When the inclination angle is 45°, rock samples have small peak stress. Peak stress decreases rapidly with the increase in impacts. The internal crack structure of rock samples and the impact number of disturbances are important factors affecting the ability of rocks to resist external impacts. The crack structure leads to the difference in the propagation path and form of internal microcracks; the impacts of disturbances cause accumulated damages. The variation law of dynamic peak stress of rock samples with different inclination angles is consistent with that of the dynamic deformation modulus.


Figure 11. Relationship between dynamic peak stress and disturbance impact times.

3.4. Rock Failure Mode

Under impacting disturbances, the crack ends are damaged at first and eventually develop into tensions and shear failure. Tensile failure is expressed as wing cracks, which usually originate at cracks' ends and gradually develop approximately parallel to the loading direction. Shear failure is mainly expressed as anti-wing and secondary coplanar cracks. Anti-wing cracks are opposite to wing cracks in the initiation direction and develop in the opposite direction to wing cracks. Secondary coplanar cracks also originate at the cracks' ends and develop coplanar with cracks [25]. NMR imaging technology was used to determine the previous internal pore distribution of rock samples before cracks. After that, the surface cracks were depicted on fractured rock samples to compare the crack propagation modes of rock samples with different crack inclination angles under impact loads. Figure 12 shows the failure modes of rock samples with different inclination angles.

After impacting disturbances, the scattered bright spots increase at the two crack ends of rock samples with the crack inclination angle of 0° and are connected to become a strip-shaped area. The remaining bright spots are randomly distributed at both ends of rock samples (see Figure 12). Most are distributed in the lower part, indicating that internal damages of rock samples increase significantly after being subjected to impact loads. The failure state and crack distribution of rock samples show that rock samples with horizontal cracks generate radial tensile stress under axial compressive stress, which forms a tensile crack penetrating the bottom end at the crack ends of rock samples. Cracks are almost parallel to the axial stress direction, representing brittle splitting failure.

Rock samples with a crack inclination angle of 30° have strip-shaped continuous bright spots near loading ends and crack tips. More small pores at both ends of rock samples and cracks are connected to form surface cracks. Affected by tensile stress, rock samples generate wing cracks in the upper part of prefabricated cracks to connect the upper ends of rock samples. At the ends of the centrosymmetric prefabricated cracks, the other anti-wing crack develops toward the upper ends of rock samples, with an initiation angle of about 104°.
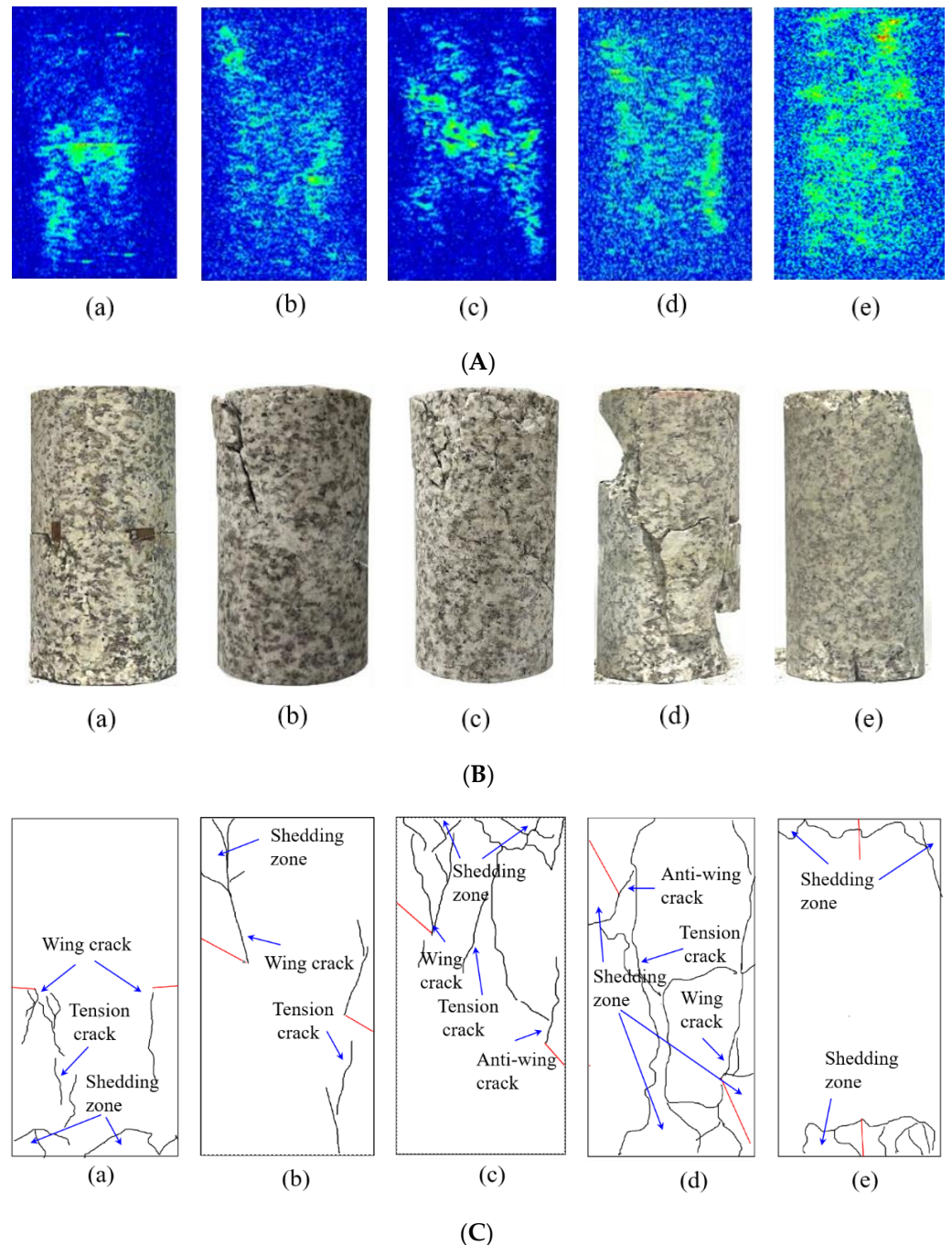
Figure 12. Failure modes of rock samples with different crack inclination angles at dynamic impact loadings: (**A**) pore distribution; (**B**) failure characteristics of rock samples; (**C**) crack distribution ((a) $\beta = 0°$, (b) $\beta = 30°$, (c) $\beta = 45°$, (d) $\beta = 60°$, (e) $\beta = 90°$).

There are multiple axial strip-shaped continuous bright spots inside rock samples with a crack inclination angle of 45°. According to the distribution of surface cracks of rock

samples, the two anti-wing cracks are developed at both ends of prefabricated cracks. Wing cracks are developed on the left side; tension cracks are formed above rock samples. The initiation angle of two anti-wing cracks approximates 128°. Many shedding areas exist in the upper parts of rock samples. However, the lower parts have good integrity.

There are multiple axial strip-shaped continuous bright spots inside rock samples with a crack inclination angle of 60°. Combined with the surface cracks of rock samples, two wing cracks and two anti-wing cracks are developed at both ends of prefabricated cracks, forming two tension cracks penetrating up and down. The initiation angle of two anti-wing cracks approximates 142°. Prefabricated cracks fall off severely and rock samples are broken as a whole due to multiple impacts.

Rock samples with a crack inclination angle of 90° have large shedding areas at the upper and lower ends. The upper right part falls, and no obvious crack development is observed at the ends of prefabricated cracks. During the multiple cyclical impacts of rock samples, no obvious surface cracks are found in the middle of rock samples except for exfoliation failure at the end.

3.5. Change Laws of Porosity

Natural granites contain a large amount of primary damage. It is impossible to ensure the same primary damage to all rock samples during preparation. Therefore, damage changes cannot be simply calibrated by the increased value of porosity. The change rate of porosity is used to calibrate the internal-damage changes of rock samples before and after the SHPB impact, which reduces individual differences in rock samples. Changes in porosity can be expressed as:

$$\alpha = \frac{K_c - K_y}{K_c} \tag{5}$$

where α is the change in porosity, K_y is the original porosity of rock samples, and K_c is the porosity of rock samples after impacts.

Figure 13 shows the changing curves of rock samples' porosity with different inclination angles of cracks.
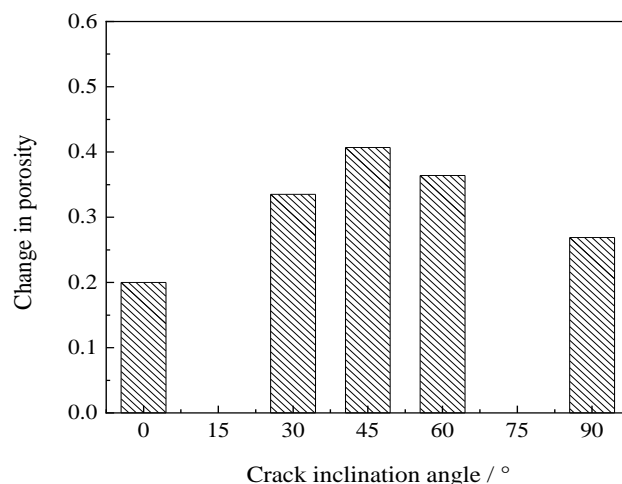
Figure 13. Changing curves of rock samples' porosity with different inclination angles of cracks.

The damage degrees of rock samples with different crack inclination angles are sequenced from high to low (45° > 60° > 30° > 90° > 0°), presenting "inverted U-shaped" distribution. Rock samples with crack inclination angles of 45 and 0° have the maximum and minimum damages, respectively. When the angle between the crack surface and impact stress direction is 30–60°, cracks are significantly developed. Then, small cracks of rock samples are connected, generating macroscopic damage.

4. Analysis and Discussion

4.1. Energy Density per Unit Time Analysis

In the failure process of rock samples, energy transformation and dissipation can macroscopically explain the failure mechanism of rocks. According to the one-dimensional stress theory, incident wave energy E_I, reflected wave energy E_R, and transmitted wave energy E_T can be expressed as

$$
\begin{aligned}
E_I &= A_0 c_0 E_0 \int_0^t \varepsilon_i^2(t) \mathrm{d}t \\
E_R &= A_0 c_0 E_0 \int_0^t \varepsilon_r^2(t) \mathrm{d}t \\
E_T &= A_0 c_0 E_0 \int_0^t \varepsilon_t^2(t) \mathrm{d}t
\end{aligned}
\tag{6}
$$

Ignoring energy attenuation of the stress wave propagating in the rod and the energy lost at the interface between the pressure rod and rock sample, E_I is converted into E_R, E_T, and dissipated energy E_D in the impacting disturbance experiment.

$$
E_I = E_R + E_T + E_D \tag{7}
$$

Dissipated energy per unit volume is used to characterize stress wave energy absorbed by rock samples, which eliminates the effect of rock samples' sizes and stress wave durations on dissipated energy [26]. The energy density per unit time is expressed as dissipated energy per unit volume within unit time to judge the energy dissipation of rocks (see Equations (7) and (8)). In the test, the start and end times of the reflected and transmitted waves are consistent. The experience time of the reflected wave is used as the action time of the stress wave in rock samples.

$$
E_V = E_D / V_s \tag{8}
$$

$$
E_{VT} = E_D / (V_s \cdot T_R) \tag{9}
$$

where E_V is the dissipated energy per unit volume, E_{VT} is the energy density per unit time, V_S is the volume of rock samples, and T_R is the elapsed time of reflected waves.

According to the elapsed time of reflected waves of rock samples with crack inclination angles of 0–90°, the energy density per unit time is calculated by Equation (9) to obtain the relationship between the energy density per unit time and impact times (see Figure 14). The average dissipated energy of the same rock samples at different impact times can be calculated to obtain the relationship between the energy density per unit time and the crack inclination angle (see Table 1).
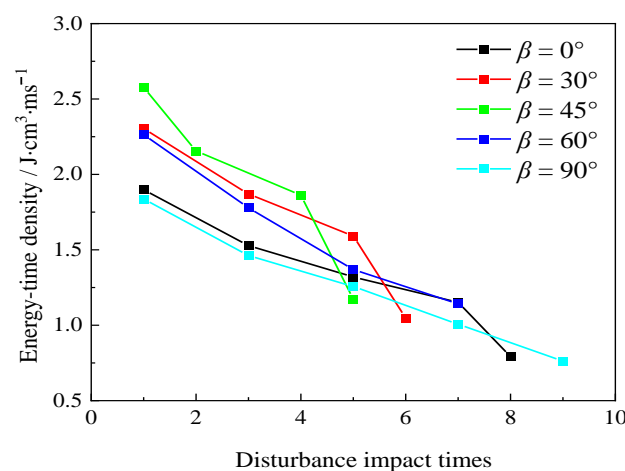

Figure 14. Relationship between the energy density per unit time and impact times.

Figure 14 shows that the energy density per unit time of rock samples gradually decreases with the increase in impacts. For rock samples with crack inclination angles

of 0–45°, energy dissipation slowly develops during the cyclic impact process where the main increment is caused by the last impact failure. Table 1 shows that energy density per unit time E_{vt} of rock samples with crack inclination angles of 0–90° decreases after increasing with the increase in angle. When the inclination angle ranges from 0 to 45°, E_{vt} rises from 1.33 to 1.94 J·cm^3·ms^{-1}, and energy absorbed by rock samples continues to increase. When the inclination angle is 45°, the energy absorption reaches the highest level. When the inclination angle ranges from 45 to 90°, E_{vt} decreases to the minimum of 1.25 J·cm^3·ms^{-1}, and absorbed energy gradually decreases. When the inclination angle ranges from 30 to 60°, E_{vt} significantly changes. This indicates that the fractured rock samples absorb more incident energy, which is consumed by crack initiation and expansion under impacts.

Table 1. Energy densities per unit time of rock samples with different crack inclination angles.

Crack Inclination Angle β (°)	Average Energy Consumption E_D (J)	Sample Volume vs. (cm^3)	Reflected Wave Time T_R (ms)
0°	43.19	195.67	0.165
30°	50.86	196.46	0.152
45°	54.32	197.05	0.142
60°	49.21	196.30	0.153
90°	40.73	197.28	0.164

Data show that the energy density per unit time and the crack inclination angle appear parabolic, which is consistent with the relationship between the average change rate of porosity and the crack inclination angles in Figure 13. The peak strength law of rock samples with different inclination angles shows that rock samples with higher strength consume more energy in the crack initiation and propagation process under the same impact load.

4.2. Characteristic Analysis of the Deformation Modulus

The deformation modulus reflects the characteristic quantity of stress when rocks produce unit strain. It is an important parameter characterizing the deformation of rocks against external impact loads. In the dynamic-deformation modulus analysis in Section 3.2, the average dynamic deformation modulus can reflect the overall deformation characteristics of rocks at the impact stage. However, the phase change characteristics of the deformation modulus are easily ignored during a single impact because of the difference between the first and second secant moduli (see Figure 8). Therefore, the phase change characteristics of two deformation moduli are analyzed for rock samples with crack inclination angles of 0–90° during successive impacts.

The first-type secant modulus proposed by C. E. Fairhurst and J. A. Hudson [27] and the second-type secant modulus proposed by Gong et al. [7] are defined as follows:

$$E_{0.5}^1 = \frac{\sigma_{0.5}}{\varepsilon_{0.5}} \tag{10}$$

$$E_{0.5}^2 = \frac{\sigma_p - \sigma_{0.5}}{\varepsilon_p - \varepsilon_{0.5}} \tag{11}$$

where $\sigma_{0.5}$ and $\varepsilon_{0.5}$ are stress and strain corresponding to 50% of peak stress in the stress–strain curve, respectively.

Figure 15 shows the changing trend of the dynamic deformation modulus of granites under different impact times.

Granites have a large first secant modulus and discrete data points. The second secant modulus reflects the ratio of stress to strain in the second half of the stress–strain curve in the dynamic loading process. At the stable stage, the changing trend is consistent with the average dynamic deformation modulus of rock samples (see Figure 15). The elastic and plastic deformations of rocks are integrated into the first half. The first dynamic deformation

modulus characterizes the deformation at the plastic stage. In the dynamic loading process, the deformation modulus is discrete in the first half of the stress–strain curve.
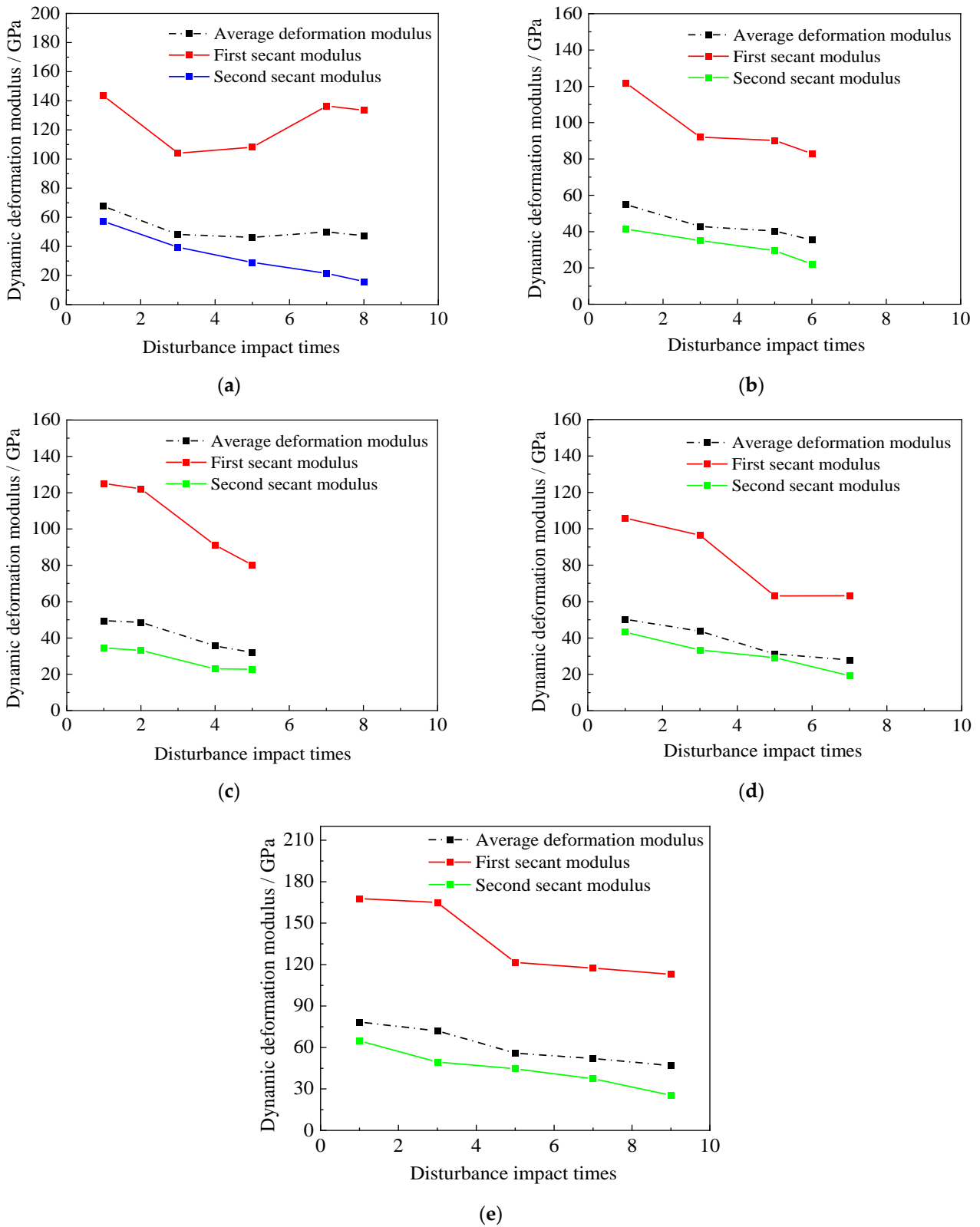
Figure 15. Change trend of the dynamic deformation modulus of granite: (**a**) $\beta = 0°$; (**b**) $\beta = 30°$; (**c**) $\beta = 45°$; (**d**) $\beta = 60°$; (**e**) $\beta = 90°$.

Rock samples are produced by cutting prefabricated cracks on intact brittle granites. Prefabricated cracks are closed in certain cycles when there are visible small cracks at crack tips. The incident wave reflects on the new crack surfaces to produce tensile waves, which aggravates the expansion, nucleation, and aggregation of microcracks. The bearing capacity of rocks decreases to reduce the elastic modulus in the second half at the loading stage. Therefore, there is a large difference between the first and second secant moduli in studying failure characteristics of fractured rock masses. However, the experimental results also reflect the deformation and failure characteristics of fractured rock masses to a certain extent.

4.3. Rock Failure Mechanism

When the number of impacts reaches a certain value, the completely closed microcracks inside the rock slowly expand from the crack tip. When there is a certain angle between cracks and loading stress, the cracks at crack tips are most active in producing more microcracks. The fracture zone composed of these microcracks is gradually connected with the local fracture zone at the loading end along the loading direction, thus causing the overall instability and failure of rocks. Based on the failure modes of different rock samples (see Figure 12), rock samples with inclination angles of 30°, 45°, and 60° have more strip-shaped continuous bright spot areas than those with inclination angles of 0° and 90°. The internal cracks in rock samples with inclination angles of 30°, 45°, and 60° develop faster under impact disturbances.

Rock samples with inclination angles of 0° and 90° are mainly affected by tensile stress producing tensile or splitting failure. For rock samples with the inclination angle of 0°, wing cracks originate in the middle of cracks. Rock samples with the inclination angle of 90° are spalled near the prefabricated crack, without wing or anti-wing cracks. Rock samples with a certain inclination angle are subjected to tensile–shear failure. In addition, the shear failure gradually dominates with the increased inclination angle. When inclination angles are 45–60°, rock samples have the weakest impact resistance and most serious shear failure.

The same rock materials were used to make fractured rock samples with different inclination angles, and scattered spots were drawn on rock surfaces to further compare the differences in the failure mechanism of rock samples under dynamic and static loadings The static uniaxial loading test of fractured rock samples was carried out using the WEP-600 hydraulic-screen universal testing machine, and the deformation and failure characteristics of the whole process were monitored by the three-dimensional digital image correlation (3D-DIC) system. During the test, the displacement control was adopted first, and the axial force control was adopted after loading to 1 KN. The loading rate of the axial force was 0.5 KN/s until the specimen was damaged. Figure 16 shows the failure forms of rock samples with different crack inclination angles under the same loading.

(a)　　　　　(b)　　　　　(c)　　　　　(d)　　　　　(e)
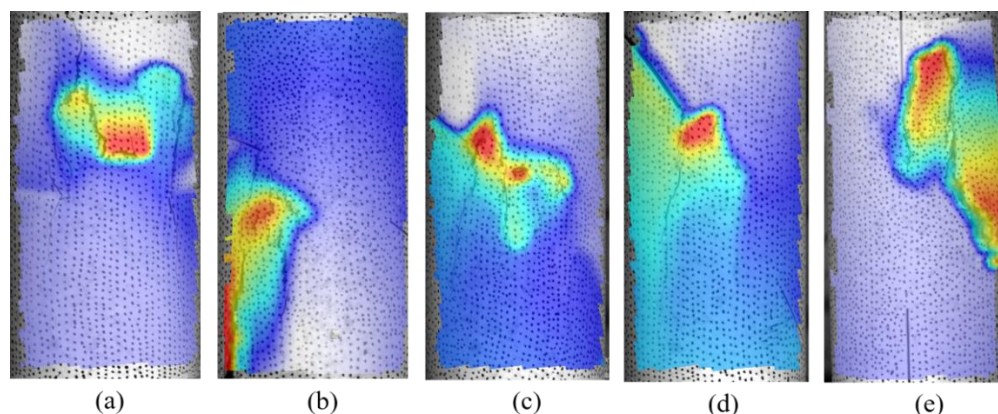
Figure 16. Failure modes of rock samples with different rock-bridge inclination angles under static loading: (**a**) $\beta = 0°$, (**b**) $\beta = 30°$, (**c**) $\beta = 45°$, (**d**) $\beta = 60°$, (**e**) $\beta = 90°$.

Figure 16 shows that at the initial stage of propagating microcracks in rocks under static loading, cracks also start at crack tips, and the fracture guiding effect is the most significant for rock samples with inclination angles of 0–60°. When crack inclination angle is 0°, transverse tensile stress is generated under uniaxial compression, and rocks are prone to tensile failure. Since the compressive capacity of rocks is much higher than their tensile capacity, rocks do not produce shear failure. When the inclination angles are 30–45°, compressive stress and tensile stress are generated simultaneously. This promotes the sliding failure of rocks along the microfracture surface, with shear failure and tensile failure occurring. When inclination angles are 60–90°, shear stress on the failure surface exceeds the limit that rocks can bear. Rocks slip along the fracture surface, mainly exhibiting shear failure.

According to the change law, the deformation modulus of rock samples has a short period of stable development during cyclic impacting disturbances. This is manifested by the slow decrease in the deformation modulus during certain impacts. For rock samples with different crack inclination angles, the appearance times and significance are different (see Figure 15). For the samples with inclination angles of 0° and 30°, the period significantly appears at the medium stage of impacts. For the rock samples with crack inclination angles of 45°, 60° and 90°, the period appears at the early and late stages of impacts. Namely, the deformation modulus changes greatly at the medium stage of impacts. Internal microcracks of rock samples accumulate and are penetrated, which causes severe brittle deformation failure. Therefore, the impact resistance of rocks continues to decrease with the increase in cumulative damages. For rock samples with a short stable development period of the deformation modulus, the second secant modulus rapidly decreases at the late stage.

5. Conclusions

(1) In the axial loading–dynamic disturbance test, dynamic deformation moduli and peak stress decreased with the increase in impacts, leading to the deterioration of rock strength. The average strength was used to reflect the ability of rocks to resist frequent impacting disturbances. The average strength gradually decreased with the increase in impacts in a linear relationship. For fractured rock masses, the dynamic deformation modulus and peak stress increased after decreasing with the increase in crack inclination angle.

(2) The crack inclination angles affected the failure characteristics of rocks. Fractured rock samples with inclination angles of 0° and 90° mainly exhibited tensile failure or splitting failure; samples with inclination angles of 30–60° mostly exhibited tensile–shear damages. With the increase in inclination angle, the shear failure gradually dominated. The initiation angle of wing cracks gradually decreased with the increase in inclination angle.

(3) Measurement of microscopic damages of fractured rocks showed that crack inclination angles and the average change rate of porosity were roughly parabolic. This was consistent with the change law of energy density per unit time and opposite to that of the average strength.

(4) Under disturbance loads, the energy density per unit time of rock samples changed in an "inverted U-shape" with the increase in crack inclination. When the critical angle between cracks and loading surfaces reached 45°, cumulative damages to rocks were most significant. Therefore, the influence of the orientation of discontinuity in rock masses on their stability should be emphasized in the practice of fractured rock mass engineering.

References

1. Cerfontaine, B.; Collin, F. Cyclic and fatigue behaviour of rock materials: Review, interpretation and research perspectives. *Rock Mech. Rock Eng.* **2018**, *51*, 391–414. [CrossRef]
2. Yang, F.J.; Hu, D.W.; Zhou, H.; Lu, J.J. Physico-mechanical behaviors of granite under coupled static and dynamic cyclic loadings. *Rock Mech. Rock Eng.* **2020**, *53*, 2157–2173. [CrossRef]
3. Xie, H.P.; Zhu, J.B.; Zhou, T.; Zhang, K.; Zhou, C.T. Conceptualization and preliminary study of engineering disturbed rock dynamics. *Geomech. Geophys. Geo-Energy Geo-Resour.* **2020**, *6*, 34. [CrossRef]
4. Zhao, Y.L.; Zhang, L.Y.; Wang, W.J.; Wan, W.; Li, S.Q.; Ma, W.H.; Wang, Y.X. Creep behavior of intact and cracked limestone under multi-level loading and unloading cycles. *Rock Mech. Rock Eng.* **2017**, *50*, 1409–1424. [CrossRef]
5. Li, X.B.; Gu, H.L.; Tao, M.; Peng, K.; Cao, W.Z.; Li, Q.Y. Failure characteristics and meso-deterioration mechanism of pre-stressed coal subjected to different dynamic loads. *Theor. Appl. Fract. Mech.* **2021**, *115*, 103061. [CrossRef]
6. Gong, F.Q.; Hu, J.P. Energy dissipation characteristic of red sandstone in the dynamic brazilian disc test with SHPB setup. *Adv. Civ. Eng.* **2020**, *2020*, 7160937. [CrossRef]
7. Gong, F.Q.; Si, X.F.; Li, X.B.; Wang, S.Y. Dynamic triaxial compression tests on sandstone at high strain rates and low confining pressures with split Hopkinson pressure bar. *Int. J. Rock Mech. Min. Sci.* **2019**, *119*, 211–219. [CrossRef]
8. Jin, J.F.; Li, X.B.; Qiu, C.; Tao, W.; Zhou, X.J. Evolution model for damage accumulation of rock under cyclic impact loadings and effect of static loads on damage evolution. *Chin. J. Rock Mech. Eng.* **2014**, *33*, 1662–1671. (In Chinese)
9. Tian, N.C.; Wang, Z.L.; Xiong, F.; Liu, Z.Y. Influence of axial pressure on dynamic mechanical properties of granite under cyclic impact loading. *J. Harbin Inst. Technol.* **2021**, *53*, 156–164. (In Chinese)
10. Wang, Z.L.; Yang, H.; Tian, N.C. Mechanical property and damage evolution mechanism of granite under uniaxial cyclic impact. *J. Harbin Inst. Technol.* **2020**, *52*, 59–66. (In Chinese)
11. Liu, H.Y.; Huang, Y.S.; Li, K.B.; Zhang, J.H. Test study of strength and failure mode of pre-existing jointed rock mass. *Rock Soil Mech.* **2013**, *34*, 1235–1241, 1246. (In Chinese)
12. Zhou, Y.; Wu, S.C.; Gao, Y.T.; Misra, A. Macro and meso analysis of jointed rock mass triaxial compression test by using equivalent rock mass (ERM) technique. *J. Cent. South Univ.* **2014**, *21*, 1125–1135. [CrossRef]
13. Guo, Q.F.; Wu, X.; Cai, M.F.; Xi, X.; Ren, F.H.; Miao, S.J. Experiment on the strength characteristics and failure modes of granite with pre-existing cracks. *Chin. J. Eng.* **2019**, *41*, 43–52. (In Chinese)
14. Zhou, X.P.; Zhang, J.Z.; Berto, F. Fracture Analysis in Brittle Sandstone by Digital Imaging and AE Techniques: Role of Flaw Length Ratio. *J. Mater. Civ. Eng.* **2020**, *32*, 4020085. [CrossRef]
15. Sun, B.; Luo, Y.; Xie, J.H.; Zeng, S. Crack propagation characteristics of jointed rock mass under static and dynamic loads. *J. Univ. South China Sci. Technol.* **2018**, *32*, 37–42. (In Chinese)
16. Wang, Q.Z.; Xia, K.W.; Wu, B.B.; Xu, Y.; Liu, F. Dynamic failure of simulated rock mass plate containing two parallel cracks. *J. Tianjin Univ. Sci. Technol.* **2019**, *52*, 1099–1108. (In Chinese)
17. Li, D.Y.; Han, Z.Y.; Sun, X.L.; Li, X.B. Characteristics of dynamic failure of marble with artificial flaws under split Hopkinson pressure bar tests. *Chin. J. Rock Mech. Eng.* **2017**, *36*, 2872–2883. (In Chinese)
18. Li, D.Y.; Wang, T.; Cheng, T.J.; Sun, X.L. Static and dynamic tensile failure characteristics of rock based on splitting test of circular ring. *Trans. Nonferr. Met. Soc. China* **2014**, *26*, 1912–1918. [CrossRef]
19. Yang, S.Q.; Ranjith, P.G.; Huang, Y.H.; Yin, P.F.; Jing, H.W.; Gui, Y.L.; Yu, Q.L. Experimental investigation on mechanical damage characteristics of sandstone under triaxial cyclic loading. *Geophys. J. Int.* **2015**, *46*, 846–866. [CrossRef]
20. Chen, R.; Li, K.; Xia, K.W.; Lin, Y.L.; Yao, W.; Lu, F.Y. Dynamic fracture properties of rocks subjected to static pre-load using notched semi-circular bend method. *Rock Mech. Rock Eng.* **2016**, *49*, 3865–3872. [CrossRef]

21. Dai, F.; Huang, S.; Xia, K.W.; Tan, Z.Y. Some fundamental issues in dynamic compression and tension tests of rocks using split hopkinson pressure bar. *Rock Mech. Rock Eng.* **2010**, *43*, 657–666. [CrossRef]

22. Gong, F.Q.; Wu, C. Identifying crack compaction and crack damage stress thresholds of rock using load-unload response ratio (LURR)theory. *Rock Mech. Rock Eng.* **2020**, *53*, 943–954. [CrossRef]

23. Zhu, Q.Q.; Li, D.Y.; Wang, W.J. Mechanical behavior and permeability evolution of sandstone with confining pressure after dynamic loading. *Geomech. Geophys. Geo-Energy Geo-Resour.* **2021**, *7*, 81. [CrossRef]

24. Jian, W.B.; Xu, X.T. Study on Damage Deterioration of Rock Slope under Dynamic Loads. *Landslide Sci. Safer Geoenviron.* **2014**, *2014*, 107–113.

25. Sagong, M.; Bobet, A. Coalescence of multiple flaws in uniaxial compression. In Proceedings of the 4th North American Rock Mechanics Symposium, Seattle, WA, USA, 31 July–3 August 2000; pp. 1203–1210.

26. Zhao, G.Y.; Li, Z.Y.; Wu, H.; Wang, E.J.; Liu, L.L. Dynamic failure characteristics of sandstone with non-penetrating cracks. *Rock Soil Mech.* **2019**, *40* (Suppl. S1), 73–81. (In Chinese)

27. Fairhurst, C.E.; Hudson, J.A. Draft ISRM suggested method for the complete stress-strain curve for intact rock in uniaxial compression. *Int. J. Rock Mech. Min. Sci.* **1999**, *36*, 279–289.